Materials Science & Engineering A 950 (2026) 149552

Contents lists available at ScienceDirect

Materials Science & Engineering A

journal homepage: www.elsevier.com/locate/msea

Deformation-induced martensitic transformation in fused filament fabrication austenitic stainless steels during tension at wide range of temperatures (77 K, RT)

J. Tabin [a,*], J. Kawałko [b], D. Schob [c], R. Roszak [d,e], A. Brodecki [a], P. Bała [b,f], Ph Maasch [c], Z. Kowalewski [a], M. Ziegenhorn [e]

[a] Institute of Fundamental Technological Research, Polish Academy of Sciences, 02-106, Warsaw, Poland
[b] Academic Centre for Materials and Nanotechnology, AGH University of Krakow, 30-059, Krakow, Poland
[c] Department 9.6 Additive Manufacturing of Metallic Components, Bundesanstalt für Materialforschung und -prüfung (BAM), 12205, Berlin, Germany
[d] Chair of Engineering Mechanics and Machine Dynamics, Brandenburg University of Technology Cottbus-Senftenberg, Senftenberg, Germany
[e] Institute of Applied Mechanics, Poznan University of Technology, Poznan, Poland
[f] Faculty of Metals Engineering and Industrial Computer Science, AGH University of Krakow, 30-059, Krakow, Poland

ARTICLE INFO

Keywords:
TRIP effect
Fused filament fabrication
316L
Cryogenic temperatures
Microstructure

ABSTRACT

This study investigates the mechanical behaviour of fused filament fabrication (FFF) of 316L austenitic stainless steel compared to conventional 316L at room temperature and 77 K, focusing on deformation-induced martensitic transformation (DIMT). Results reveal that the Lüders-like effect, present in conventional 316L at 77 K, is absent in FFF 316L due to porosities that hinder martensitic front propagation. At room temperature, uniform strain distribution and DIMT were observed in conventional 316L, whereas in FFF 316L, martensitic nucleation occurred around pores, serving as a localized strengthening mechanism. Microstructural analysis identified Fe-δ islands along grain boundaries in FFF 316L, which contribute to its multiphase nature. Although FFF 316L demonstrates lower yield stress and elongation compared to conventional 316L, this study does not establish design allowables. The present findings are limited to monotonic tensile behaviour, fatigue performance and corrosion resistance under cryogenic conditions were not assessed. Further optimization of fabrication parameters to minimize ferrite content and porosities is suggested to enhance mechanical performance.

1. Introduction

Austenitic stainless steel (ASS) 316L is widely used in various industrial applications because of its outstanding corrosion resistance, high ductility, and good mechanical properties, especially under extreme temperature conditions. ASS was chosen for the Spacecraft due to its high strength, excellent high-temperature resistance, corrosion resistance, and durability at wide range of temperature. These properties are critical for interplanetary travel, reusability, and preserving the structural integrity of the spacecraft throughout its missions, even under extreme conditions where temperatures drop below 77 K. The components of the spacecraft fuselage, including the engine, exhaust components, landing gear components, and key superstructure joints, are made from conventional ASS. However, less critical elements could be made from 3D-printed steel. This would allow for optimized shapes and reduce material and energy consumption.

Deformation-induced martensitic transformation (DIMT) in ASS is a phenomenon where mechanical deformation leads to the transformation of the face-centered cubic (FCC) austenite phase into the body-centered cubic (BCC) or body-centered tetragonal (BCT) martensite phase [1,2]. This transformation can significantly alter the mechanical properties of the material, such as increasing strength and hardness while potentially reducing ductility. Latest findings [3] suggest that the mechanical properties of metastable FCC alloys with low to medium stacking fault energies can be effectively enhanced by facilitating martensite seeds via pre-straining at cryogenic temperatures.

This study focuses on the mechanical behaviour of 316L stainless steel, produced through both additive manufacturing (AM) and traditional manufacturing methods, with particular emphasis on deformation-induced martensitic transformation at wide range of

* Corresponding author.
E-mail address: jtabin@ippt.pan.pl (J. Tabin).

https://doi.org/10.1016/j.msea.2025.149552
Received 19 April 2025; Received in revised form 13 November 2025; Accepted 30 November 2025
Available online 1 December 2025

temperature (77 K–295 K).

Conventionally manufactured 316L has been extensively studied for cryogenic conditions [4,5]. Studies show significant differences in the deformation behaviour of ASS at cryogenic temperatures compared to room temperature [6–11]. A key process occurring in austenitic steels under mechanical stress in cryogenic conditions is DIMT [12–14]. The most frequently observed phase transformation in metastable austenitic (γ) stainless steels is the martensitic (α') transformation due to plastic deformation, which significantly influences work hardening [15–19]. This transformation typically occurs in randomly distributed, overlapping stacking faults at low stacking fault energy ($<$20 mJ m^{-2}) and has minimal effects on the macroscopic behaviour even at very low temperatures [20,21]. DIMT offers advantages such as increased strength and work hardening rates, enhancing mechanical performance under deformation [14]. On the other hand, the presence of ferrite content negatively impacts the material's properties by reducing ductile elongation, which limits its ability to undergo plastic deformation before failure. Additionally, it compromises corrosion resistance, making the material more susceptible to environmental degradation [22–24]. Furthermore, the ferrite content alters the magnetic properties of the material, introducing magnetic behaviour that may be undesirable for certain applications requiring non-magnetic performance [25,26].

In light of technological advancements, particularly in cryogenic storage and aerospace industries where complex geometries are required [27,28], AM has emerged as a promising solution for cryogenic applications. AM offers not only the advantage of producing complex geometries with minimal processing steps but also the ability to tailor the microstructure to meet specific requirements by optimizing process parameters, potentially replacing conventional ASS in such applications [29–31]. By adjusting process parameters, it is possible to control the occurrence and characteristics of DIMT in additively manufactured materials, tailoring the mechanical properties for specific applications.

Jeong et al. [32] and Hong et al. [33] have investigated the influence of laser scanning speed on DIMT, finding that a slower scanning speed delays the DIMT process, in particular during deformation at cryogenic temperatures. Increased stacking fault energy and denser cellular structures hindered the formation of shear bands, thereby suppressing martensitic transformation.

In addition to the LPBF process, the Fused Filament Fabrication (FFF) process has been in use since the 1990s. Initially introduced for the freeform fabrication of three-dimensional solid objects, this process was first applied to thermoplastics. In 1996, it was adapted for producing metal components, known as FDMet [34]. Early materials included 17-4 PH steel [35]. In recent years, research has focused on improving filament properties to achieve good extrudability at high particle loadings while maintaining the required mechanical strength. This research includes materials such as 316L stainless steel, Ti6Al4V alloy, and ceramics [36,37]. For instance, BASF has introduced the UltraFuse 316LX filament, developed for use with standard desktop FFF printers and subsequent debinding and sintering processes. A limited number of studies have been conducted on this material, focusing on aspects such as mechanical properties [38,39] corrosion resistance [29], comparison with conventionally manufactured and LPBF-produced samples [40], microstructure [41], the influence of porosity [42], build direction and printing speed [43], as well as the effects of post-processing methods such as sintering and debinding [44]. Previous investigations have been conducted exclusively at room temperature [42–44]. However, it should be noted that excellent properties at room temperature do not guarantee performance under cryogenic conditions. Therefore, this study aims to investigate the mechanical behaviour of 316L stainless steel produced via FFF and subjected to quasi-static tensile loading under cryogenic conditions. The focus lies on the effects of DIMT and how manufacturing parameters and porosity influence this transformation, as well as exploring ways to control the DIMT process.

This study seeks to compare the mechanical properties and deformation mechanisms of FFF-produced 316L with conventionally manufactured 316L. By employing tensile tests, digital image correlation (DIC), ferrite measurements, microstructural analysis using electron backscattered diffraction (EBSD), and chemical analysis using energy dispersive x-ray spectroscopy (EDS) in scanning electron microscope (SEM), this research aims to provide a comprehensive understanding of the material properties and microstructural evolution under room temperature and cryogenic conditions. The findings of this study aim to deepen the understanding of the potential of additive manufacturing to tailor the material properties of 316L, essential for developing components with enhanced properties that meet the demands of low-temperature applications and open new fields for additively manufactured metallic components [32].

2. Materials and methods

2.1. FFF process and post-processing

The Ultrafuse 316L filament, created by BASF for producing stainless steel parts through 3D printing, was employed. The schematic representation of the FFF process is shown in Fig. 1. This filament, comprising 80 % spherical metal powder and measuring 1.75 mm in diameter, facilitated the creation of "green" samples using an Ultimaker S5 desktop printer (Fig. 1a). This printer features an extruder, temperature control, a heated build plate, a movement system, and a heated print head with nozzles. For optimal adhesion and print quality, the temperature of the building platform is set to 373 K (100 °C), while the nozzle operates at a temperature of 515 K (242 °C). The printing speed is adjusted to 15 mm/s for outer layers to ensure fine detail, while inner layers are printed at a faster speed of 20 mm/s, optimizing the printing time while maintaining mechanical strength. To obtain a fully functional metallic component, the printed "green parts" must undergo debinding and sintering. During the debinding stage, the polymer binder is thermally or chemically removed, transforming the green part into a "brown part" composed of loosely bonded metallic particles. In the subsequent sintering process, these particles are metallurgically fused, producing the final "white metal part" with the desired density, dimensional accuracy, and mechanical integrity. These conventional terms—green, brown, and white—refer both to the state of the part during successive processing stages and to the visible colour changes resulting from binder removal and metallic consolidation. After final machining, the appearance and surface finish of the specimens are virtually indistinguishable from those of conventionally manufactured 316L stainless steel components.

The BASF Debinding and Sintering (D&S) process, developed for Ultrafuse 316L, consists of two main stages: removal of the polymer binder and subsequent sintering of the metallic particles. The catalytic debinding is performed in a nitrogen atmosphere (500 L/h) with nitric acid (HNO_3) dosing at 30 mL/h and a temperature of 120 °C. Under these conditions, the binder is removed from the surface at a rate of 1–2 mm/h. Debinding is considered complete once a minimum mass loss of 10.5 % is achieved, ensuring effective polymer removal without compromising the integrity of the printed part. The subsequent sintering stage densifies and strengthens the material while inducing dimensional shrinkage of approximately 16 % along the x- and y-axes and 20 % along the z-axis. Sintering is carried out in a controlled hydrogen atmosphere through multiple heat cycles: heating at 5 K/min to 600 °C with a 1 h dwell, followed by heating at 5 K/min to 1380 °C and holding for 3 h, then controlled cooling inside the sintering furnace [45]. All Ultrafuse 316L FFF printing, debinding, and sintering procedures were performed at Elnik Systems (Germany) in strict accordance with BASF's process recommendations.

Tensile specimens were manufactured according to E8 ASTM. The main dimensions of the specimens are shown in Fig. 2a. All samples were aligned on the printing plate as shown in Fig. 2b. Two different infill strategies were assessed, Fig. 2c and d. In Fig. 2c the layers were printed 0° and 90° and in case of Fig. 2d, the layers were orientated ±45°

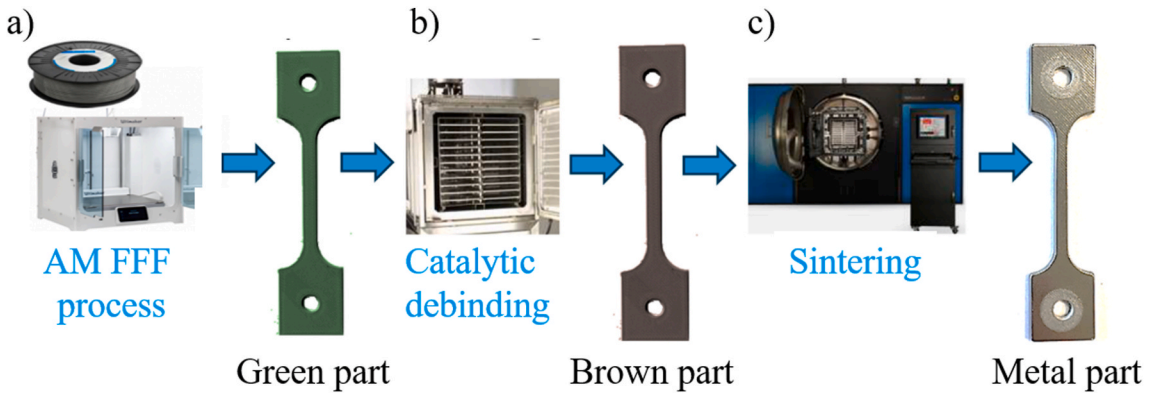

Fig. 1. Manufacturing steps: (a) printing process; (b) debinding stage; (c) sintering process.

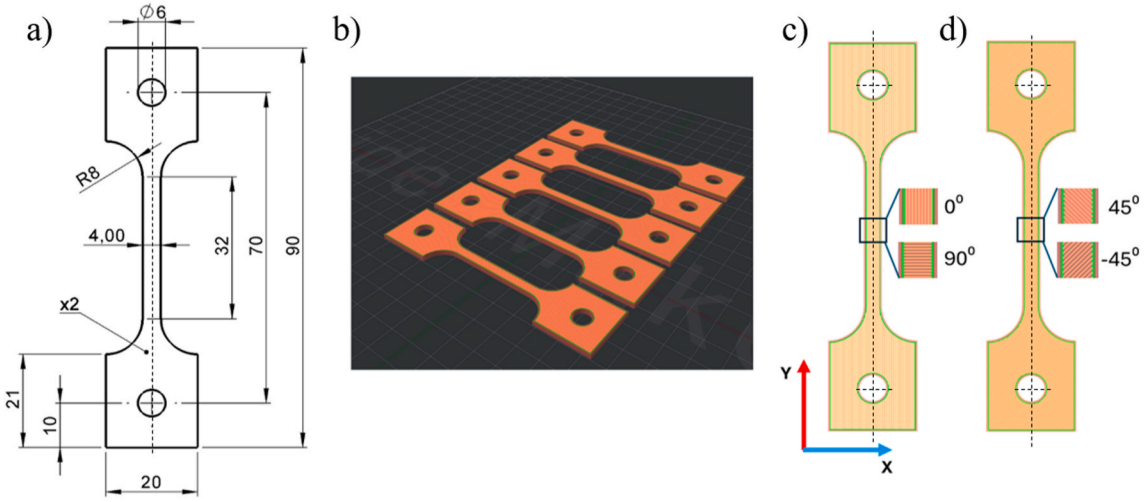

Fig. 2. Build orientation: (a) Specimen according to ASTM E8; (b) Ultimaker desktop and build orientation in (c) 45°/45° and d) 0°/90° to the tensile loading direction.

aligned to load direction. These orientations are commonly used in FFF and span the typical extremes of orientation-driven anisotropy encountered in practice [46,47]. The 0°/90° raster aligns extruded roads with the loading axis, maximizing continuous load paths and minimizing resolved shear across adjacent roads, representative of plate-like housings, covers, and fixtures, whereas the ±45° raster promotes shear-dominated load transfer with more frequent adjacent-road and interlayer interfaces, representative of brackets, frames, and general-purpose infill. This selection ties the tensile tests to application-relevant loading paths while preserving manufacturability and reproducibility.

A notable aspect of this study is the evolution of ferrite content throughout all stages of specimen fabrication (Fig. 1), following the BASF procedure (Table 1). The volume fraction of secondary phase is measured by feritscope FMP 30 (Helmut Fischer), a portable device employing magnetic induction to determine ferrite volume fraction in steel samples. Based on these measurements, the martensite volume fraction is calculated according to the methodology developed by Talonen et al. [48]. Due to the measurement limitations of the feritscope, such as the edge effect, the influence of porosity on the measurement, etc., comparing results between processes is not justified. Table 1 demonstrate that at every stage of printing, a certain amount of ferrite is present.

Table 1
Ferrite volume fraction for FFF's three-step printing process.

Printing process	Ferrite content [%]
Filament	0.30–0.60
Green part	1.22–1.36
Finished part	6.00–7.00

In addition to 3D printed parts, the study also compared these with commercial sheet 316L ASS, which are 2 mm thick. The dog bone-shaped tensile test specimens (Fig. 2a) are fabricated using electrical discharge machining (EDM) from commercial stainless-steel sheets with the tensile axis aligned with the rolling direction. The semi-products are supplied in cold-rolled and the annealed conditions according to the standards ASTM A480 and EN 10088. In these forms, the materials are typically used for structural components that operate over a wide range of temperatures. The chemical composition measured using WAS Foundry-Master optical emission spectrometer, of FFF and conventional 316L is presented in Table 2.

The microstructure investigation of steel samples was conducted using FEI Versa 3D FEG with Oxford Instruments Symmetry S2 CMOS EBSD camera, and Ultim MAX 40 EDS detector. EBSD and EDS maps were collected at beam acceleration voltage of 20 kV and probe current of 26 nA. Hough transform indexing of electron backscattered patterns (EBSP) in Oxford Aztec software was used to determine crystal orientations. The EBSD data analysis was carried out using Oxford Aztec Crystal software and Matlab with MTEX toolbox [49]. To improve the indexing rate and accuracy, a post-acquisition data treatment consisting of dynamic template matching, and orientation refinement based on stored EBSPs was performed in Aztec Crystal software. Samples for

Table 2
Chemical composition of 316L and FFF 316L samples.

Chemical composition %										
	Fe	C	Si	Mn	Ni	P	S	Cr	Mo	Al
316L	bal.	0.053	0.54	1.34	9.75	0.031	0.005	16.6	2.05	0.005
FFF 316L	bal.	0.052	0.59	1.15	10.10	0.026	0.005	16.5	2.14	0.006

microstructure investigation were mounted in resin and prepared metallographically. The metallographic preparation included grinding with SiC papers up to #2000 grit followed by mechanical polishing using diamond suspensions up to 1 μm, and final polishing step using 60 nm colloidal silica suspension in vibratory polisher.

3. Experimental results

3.1. Experimental setup and tensile test results

To investigate the material's behaviour at both cryogenic and room temperatures, an experimental setup was developed [50–52]. The cryogenic tests were conducted using a cryostat, where the specimen and transducers were mounted between the grips of a tensile test machine (Instron 1343). Liquid nitrogen (77 K) served as the cryogen, delivered into the cryostat through a transfer line until the specimen and transducers were fully immersed. A thermistor inside the cryostat monitored the cryogen level. Displacement-controlled tests were then carried out with the elongation of the specimen measured by clip-on extensometers. The general scheme of the experimental setup for cryogenic tests is illustrated in Fig. 3a.

To analyse the macroscopic behaviour of specimens and the deformation mechanism of ASS at room temperature, the Digital Image Correlation (DIC) technique is employed during the displacement-controlled tensile tests (Fig. 3b). The strain distribution during tension is monitored using the DIC Aramis 12 M system, equipped with lenses having a total focal length of 75 mm and calibrated settings suitable for the measuring area of 170 × 156 mm or 38 x 25 mm. Calibration is performed before testing using a certified GOM calibration plate.

The displacement-controlled uniaxial tensile tests are conducted on dog bone specimens of conventional 316L and FFF 316L stainless steel at room temperature and 77 K, with a crosshead velocity of 1 mm/min ($\dot{\varepsilon} = 5{,}2 \cdot 10^{-4}\, s^{-1}$). In this study, the results of the DIC analysis are presented as strain amplitude along the specimen axis for different traverse displacements (Fig. 5b). One key question arises: is it possible to quantitatively and qualitatively distinguish the differences in macroscopic strain distribution between the conventional 316L and FFF 316L steels in the initial uniform stage? To precisely examine the homogeneity of the strain field distribution in both specimens, the floating root mean square (RMS) function of strain amplitude along the symmetry axis is evaluated (Fig. 5c). This approach allows for a detailed analysis of strain distribution patterns, providing insights into the mechanical behaviour of both materials [50,53].

The martensite and ferrite volume fractions were measured using the Feritscope Fisher FMP 30, an instrument that detects all magnetic phases [48]. It is noteworthy that during the fabrication of FFF 316L, following the producer's procedure, the ferrite volume fraction varied, as shown in Table 1. The finished specimen contained approximately 6–7 % ferrite (Table 1, Fig. 3c). During tensile tests conducted at both room temperature and 77 K, no significant changes in ferrite volume fraction were observed, indicating that the ferrite islands remained stable (Figs. 9, 10d and 11d). Hence, to accurately determine the DIMT content in FFF 316L, the ferrite volume fraction was subtracted from the feritscope measurement.

The stress-strain curves from displacement-controlled tensile tests on dog bone specimens of conventional 316L and FFF 316L at room temperature and 77 K are shown in Fig. 4. At room temperature, loading-unloading tests were conducted to monitor the evolution of martensitic volume fraction across different loading cycles. These tests provide insights into the changes in material properties related to the formation of new martensitic phases throughout the cycles. At 77 K, the tests were interrupted to remove the specimen from the cryostat, and the volume fraction of martensite was measured. Subsequently, the next specimen was subjected to tension until reaching the designated plastic strain level (Fig. 6a).

Mechanical tests were repeated for each printing orientation, showing consistent yield and tensile strengths but noticeable variation in total elongation due to the brittle fracture behavior typical of additively manufactured materials at cryogenic temperatures [54]. This brittleness does not significantly affect the evolution of deformation-induced martensite, which remains uniformly distributed along the specimen axis without accumulating in the fracture region.

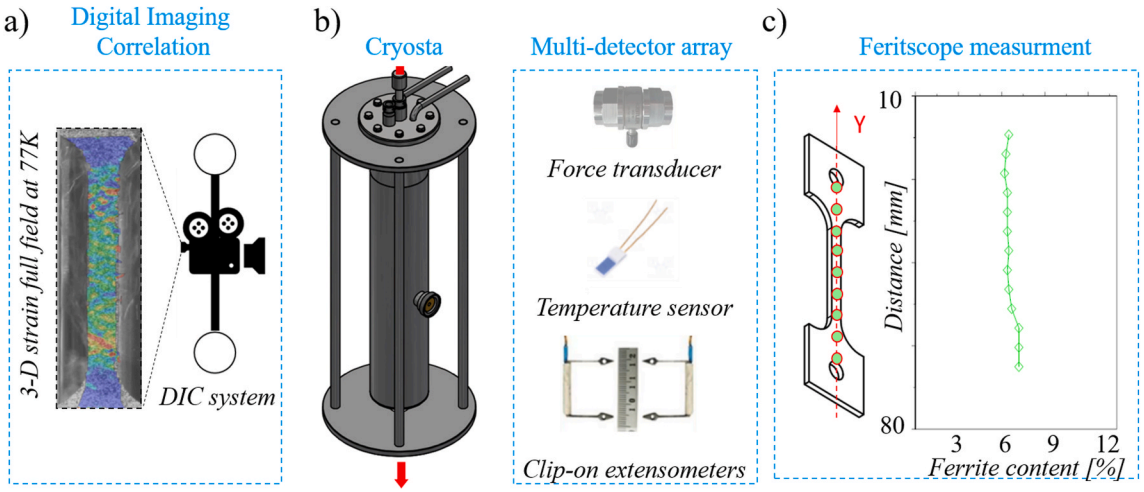

Fig. 3. Experimental setup for tensile tests at 77 K: (a) Strain evolution during uniaxial tensile test at room temperature, measured by the ARAMIS 14M system; (b) The cryostat is equipped with a force transducer, thermistors, and extensometers; (c) Ferrite volume fraction measurement along the specimen axis.

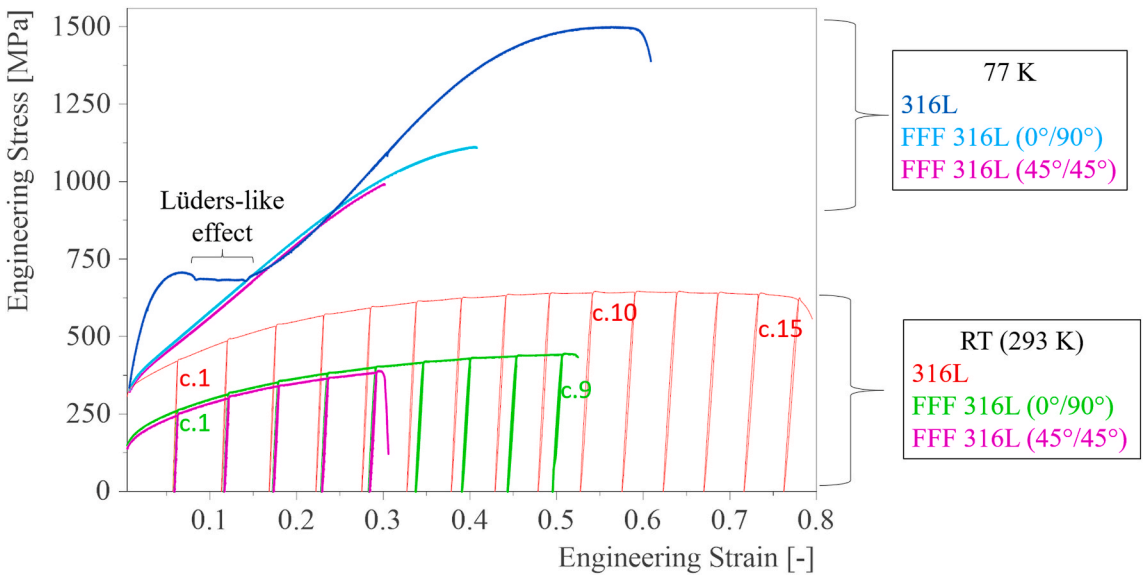

Fig. 4. Stress-strain curves for conventional 316L and FFF 316L measured at 77 K and room temperature (RT). At room temperature, loading-unloading tests were performed to observe the evolution of martensitic volume fraction across different cycles, explicitly c.1, c.9, c.10, and c.15.

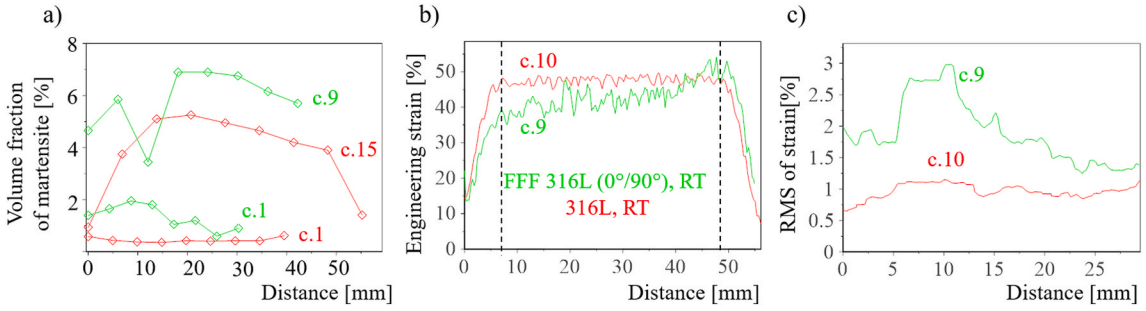

Fig. 5. (a) Evolution of deformation-induced martensitic phase in conventional 316L (red curve) and FFF 316L (0°/90°) (green curve) during loading-unloading tests at room temperature. The figure illustrates the volume fraction of martensite for the first cycle (c.1) and the last cycle (c.15) before rupture (cf. Fig. 4); (b) Strain amplitude along the specimen axis for the ninth cycle c. 9 (FFF 316L) and the tenth cycle c.10 (conventional 316L); (c) RMS-based profiles of strain calculated from strain amplitudes along the specimen axis during tensile tests of conventional 316L and FFF 316L for cycles c.10 and c.9, respectively. (For interpretation of the references to colour in this figure legend, the reader is referred to the Web version of this article.)

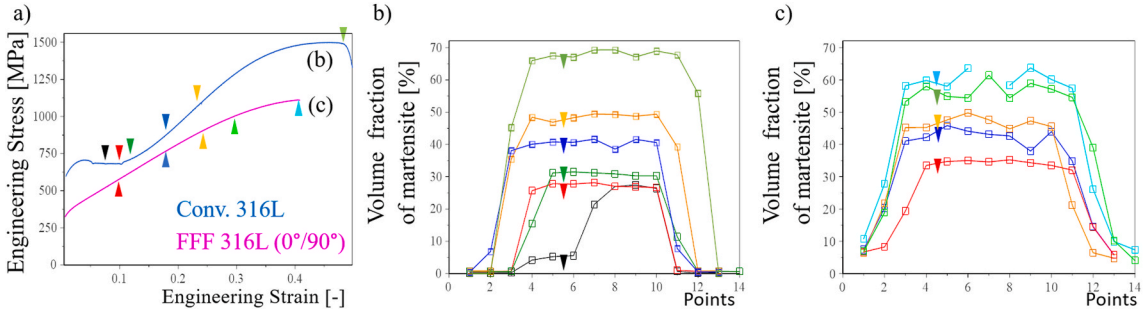

Fig. 6. (a) Uniaxial tensile tests results for conventional 316L and FFF 316L (0°/90°) at 77K (the martensite volume fraction was measured at specific plastic strain levels under cryogenic temperatures, as indicated by the triangles); (b) α′-martensite distribution along the specimen axis during a uniaxial tensile test of conventional 316L and (c) FFF 316L (0°/90°) at 77 K (colours of curves corresponds to colours of triangles). (For interpretation of the references to colour in this figure legend, the reader is referred to the Web version of this article.)

The following analysis focuses on FFF-produced 316L specimens printed in the 0°/90° orientation, as this configuration exhibits superior mechanical performance—both in terms of tensile strength and total elongation—compared to the ±45° orientation across a wide range of temperatures (Fig. 4).

3.2. *Deformation-induced martensitic transformation*

In-depth microstructural studies of the direct γ→α' as well as the two-stage γ→ε→α' phase transformation in conventional ASS have been presented in many works at a wide range of temperatures [2,12,55,56]. These studies consistently elucidate the conditions and mechanisms

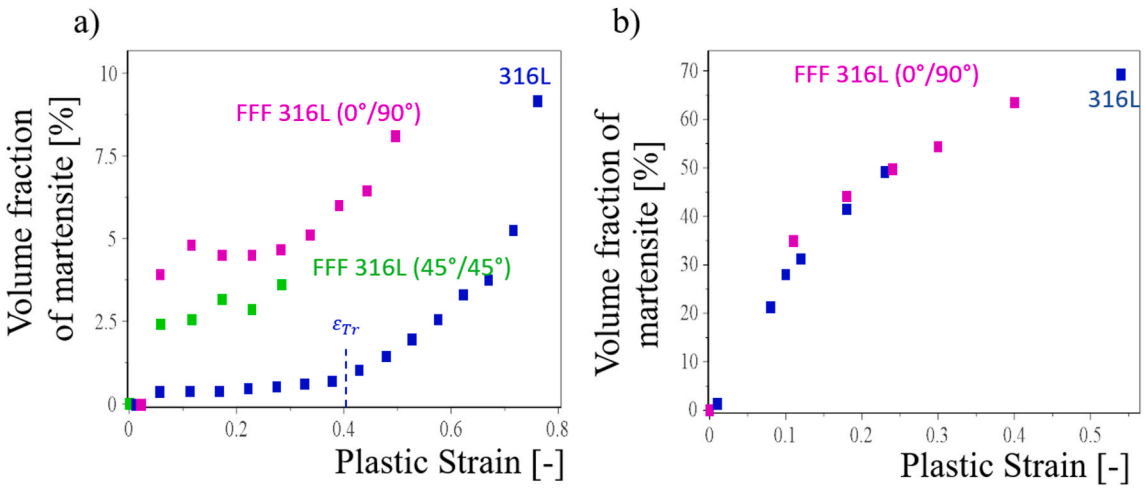

Fig. 7. Evolution of α′-martensite in conventional 316L, FFF 316L (0°/90°) and FFF 316L (45°/45°) at (a) room temperatures and (b) at 77 K.

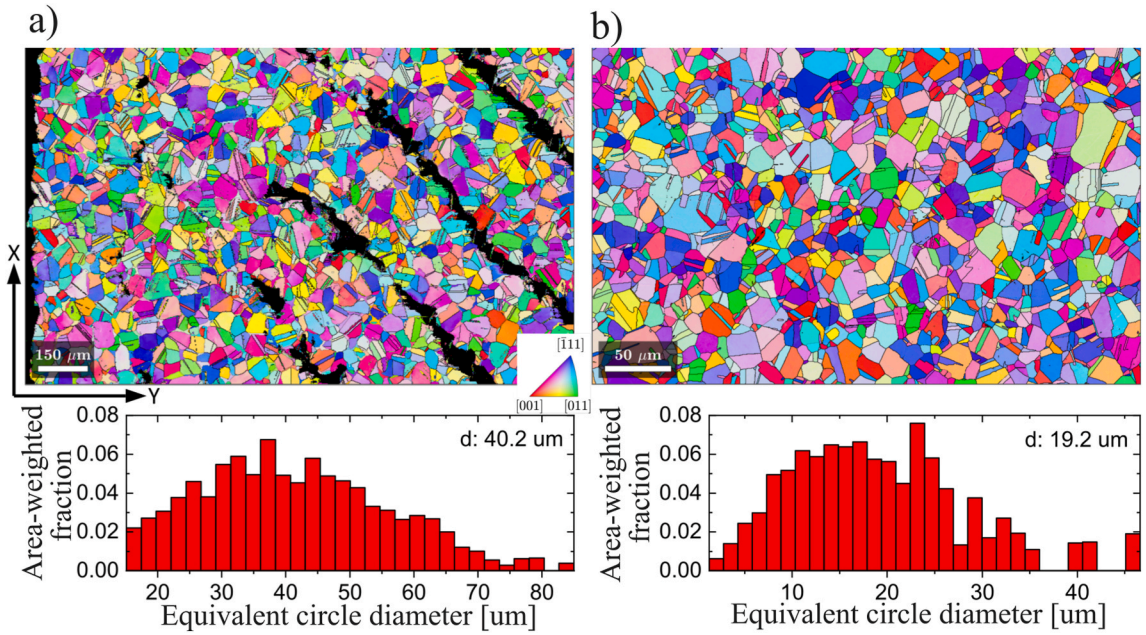

Fig. 8. Initial microstructure (before tensile testing) of the investigated materials: (a) FFF 316L and (b) conventional 316L. IPF (inverse pole figure) maps for tension direction (top row) - please pay attention to different scalebars. Grain size distributions and average values presented as diameter of equivalent circle (bottom row).

responsible for the nucleation and growth of martensite in conventional ASS. However, experimental identification of deformation-induced phase transformations in Fused Filament Fabrication remains relatively rare. Accordingly, this section presents an analysis of deformation-induced phase transformation in FFF 316L, contextualized against conventional 316L over a wide temperature range.

The evolution of DIMT was studied for conventional 316L and FFF 316L (0°/90°) at room temperature. The evolution of martensitic volume fraction along the specimen axis after 1st and 15th loading-unloading cycles is shown in Fig. 5a. To ensure accuracy, the initial ferrite volume fraction was subtracted from the feritscope measurements (Table 1). The secondary phase was measured after unloading for the first and final loading cycles (Fig. 4). The results indicate a non-uniform distribution of martensite in the FFF 316L (0°/90°) specimens. It is attributed to the non-uniform distribution of plastic strain during the uniaxial tensile test of printed specimens. To verify this, the RMS-based procedure for identifying plastic behaviour was used [50, 53]. The method utilises digital image correlation technology (DIC) to record the strain distribution during tensile testing, followed by calculating the floating root mean square (RMS) value of the strain amplitude along the specimen axis. By implementing this approach, the RMS-based profiles of strain amplitude are identified in conventional 316L and FFF 316L (0°/90°) (Fig. 5b). The RMS of strain along the specimen axis (Fig. 5c) reveals a significant strain concentration, which is considerably higher in FFF 316L than in conventional 316L samples. This indicates that the non-uniform strain distribution is accompanied by an uneven distribution of the secondary phase.

Tensile straining of conventional 316L, FFF 316L (0°/90°) and FFF 316L (45°/45°) were carried out at room temperature (Fig. 4) and at 77 K (Figs. 4 and 6a) at the strain rates $\dot{\varepsilon} = 5.2\,10^{-4}s^{-1}$. At room temperature, the volume fraction of the secondary phase was identified after unloading for each cycle. The evolution of α' – martensite as a function of plastic strain is presented in Fig. 7a. Notably, after the first loading-unloading cycle, a sharp increase in martensite volume fraction is observed in FFF 316L. In contrast, conventional 316L requires a threshold strain ($\varepsilon_{Tr} = 0.35$) before a significant increase in the

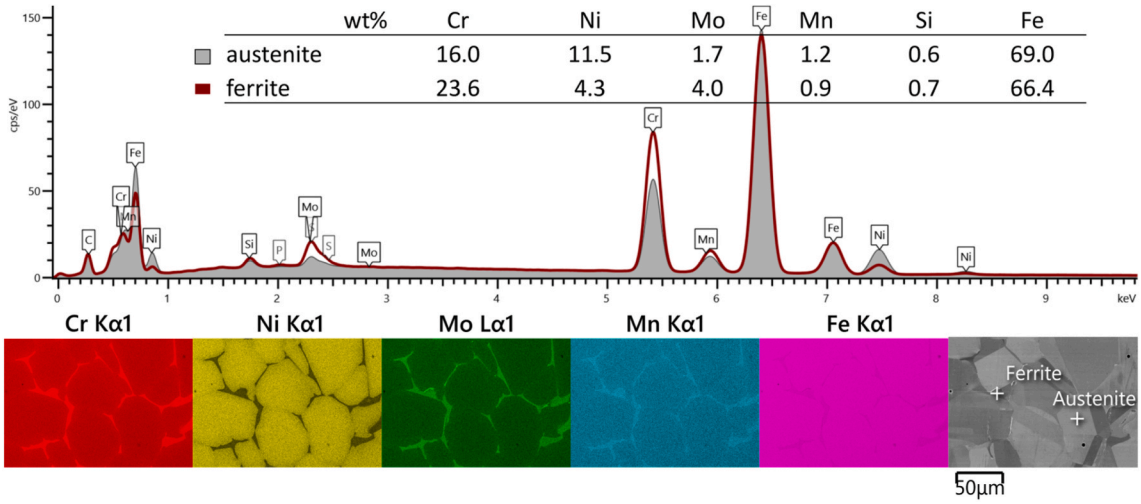

Fig. 9. Microstructure and elemental distribution EDS maps of FFF 316L sample and corresponding EDS spectra and chemical composition measured in selected austenite, and ferrite grains.

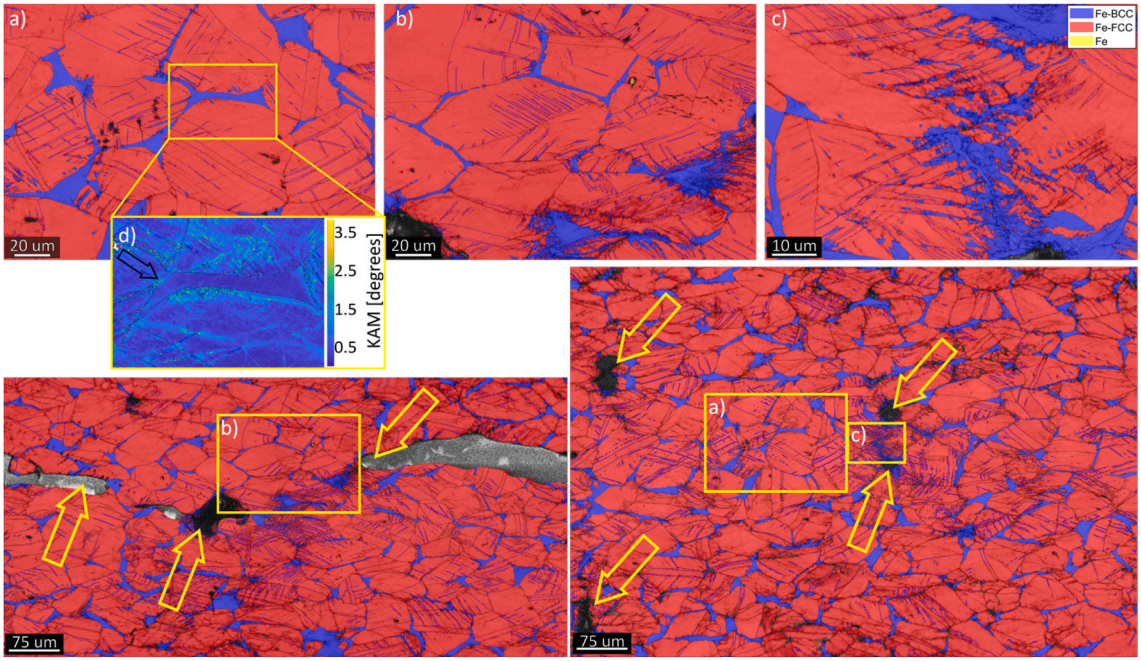

Fig. 10. Phase distribution maps of FFF 316L samples after rupture at RT: (a) deformation in bulk material; (b) and (c) deformation close to porosity; d) KAM map of the selected area, black arrow indicates deformation transport through a narrow ferrite grain; yellow arrows indicate porosity in the sintered material; blue lines indicate Σ3 boundary in austenite; red lines indicate Σ3 boundary in martensite. Please refer to full resolution image for detailed analysis. (For interpretation of the references to colour in this figure legend, the reader is referred to the Web version of this article.)

secondary phase occurs. However, the shape of the volume fraction curve is similar for both conventional and printed specimens. After fracture, the final volume fraction of martensite is comparable between FFF 316L and conventional 316L specimens. It is worth pointing out that total elongation is approximately 30 % higher in the conventional 316L specimen. One possible reason for this is the large volume fraction of delta ferrite in the FFF 316L sample. Finally, the building direction influences the kinetics of the phase transformation. For the same plastic strain level, the martensite volume fraction is higher in FFF 316L (0°/90°) compared to FFF 316L (45°/45°) (Fig. 7a).

At 77 K, the evolution of the secondary phase in both conventional 316L and FFF 316L specimens is similar (Fig. 7b). However, the conventional specimen exhibits a higher total elongation.

This variation is likely due to the enhanced transformation-induced plasticity effect seen in conventional materials (so called Lüders-like effect), which helps delay necking during uniaxial tension [57]. The evolution rate is similar in both conventional and FFF specimens, despite the initial front propagation observed in the conventional one. However, the martensitic distribution is more non-uniform for FFF 316L at both room temperature (Figs. 5a) and 77 K (Fig. 6c).

3.3. *The initial microstructure of FFF 316L and 316L steel samples*

In the initial state, the microstructure of FFF 316L steel consists of relatively large equiaxed austenite grains with an average diameter of 40 μm, in contrast to conventional 316L steel, which has a grain diameter of 19 μm (Fig. 8). The sintered FFF 316L specimens exhibit the presence of elongated macroporosity (Fig. 8), with a pattern oriented at

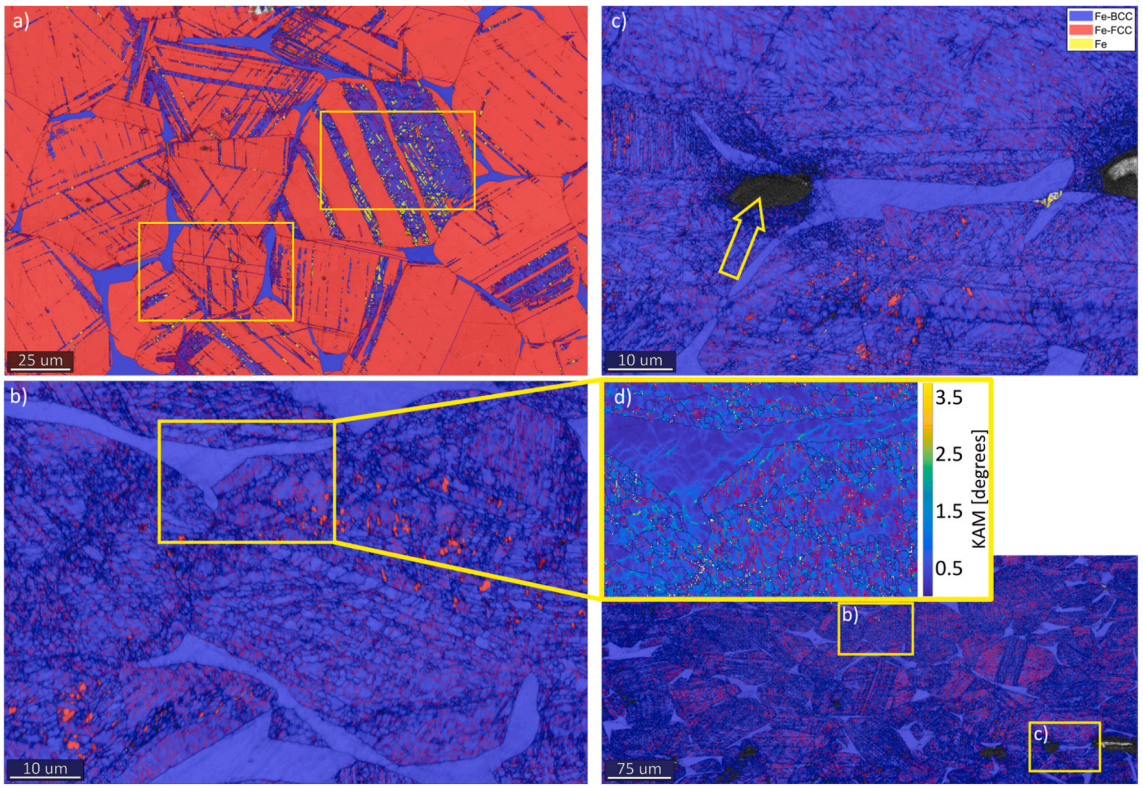

Fig. 11. Phase distribution maps of FFF 316L at 77 K: initiation of deformation (a); deformation after fracture: (b) in bulk material, (c) deformation around pores; blue lines indicate Σ3 boundary in austenite; red lines indicate Σ3 boundary in martensite, d) KAM map of selected area, indicating strong deformation of martensite and relatively low plastic deformation in a ferrite grain. Please refer to full resolution image for detailed analysis. (For interpretation of the references to colour in this figure legend, the reader is referred to the Web version of this article.)

a 45° angle in the XY plane within the bulk material (Fig. 2). Therefore, the porosity content depends on the built orientation and printing raster patterns, as it was reported by Damon et al. [42] and Santamaria et al. [58].

In both FFF 316L and conventional 316L the austenite grains appear fully recrystallized i.e. they lack any subgrain structures, including low-angle grain boundaries and internal orientation gradients. However, while conventional 316L sample exhibits a typical single-phase austenite microstructure, FFF 316L contains an additional secondary ferrite delta phase (Fe-δ). This ferrite is present in the form of islands, predominantly located at the grain boundaries and triple junctions of the austenite grains, constituting about 10 % of the microstructure.

The EDS chemical analysis (Fig. 9) reveals that ferrite islands contain higher concentrations of chromium and molybdenum (ferrite-forming elements), and lower concentrations of nickel (austenite-forming element) compared to austenite grains. It is assumed that ferrite forms from the liquid phase during the high-temperature sintering step in the manufacturing process of FFF 316L. As a result, the austenite grains have relatively lower amounts of chromium and manganese compared to conventional 316L steel. A similar two-phase microstructure is observed in 316L steel fabricated by direct laser deposition (DLD), due to crystallization from the laser-induced melt pools. Similarly, it is expected that a post-sintering heat treatment of FFF 316L for 2 h at 1150 °C would dissolve the ferrite phase and homogenize the chemical composition [59].

3.4. Microstructure evolution during tensile tests at 77 K and room temperatures

The microstructure of deformed 316L samples was investigated in several areas and at different magnifications to capture both the general material behaviour and the detailed formation of martensite within austenite grains. The FFF 316L samples were examined after being tested to failure (after final cycle as shown in Fig. 4), with EBSD measurement areas selected away from the fracture zone. In contrast, for the conventional 316L samples, the tensile test was stopped before failure, and EBSD maps were collected from regions outside and inside the plastic deformation zone.

The FFF 316L tested at room temperature demonstrates an inhomogeneous microstructure evolution. In the bulk material, deformation occurs in the austenite grains through dislocation slip and mechanical twinning. The pre-existing recrystallization twins in the austenite grains bend due to dislocation slip activity, resulting in a deviation from the ideal Σ3 ⟨111⟩ 60° misorientation (Fig. 10a). The Σ3 grain boundaries in presented EBSD maps were identified using the Brandon criterion [60], i.e. with 8.66° angle threshold deviation from ideal ⟨111⟩ 60° misorientation.

New mechanical twins appear as narrow needles. The interaction between the mechanical twins, and between mechanical twins and existing high angle grain boundaries (HAGB) results in nucleation of Fe-BCC martensite α'. The inhomogeneity is revealed by deformation localization in areas close to pores present in FFF 316L. Fig. 10b and c reveals intensification of mechanical twinning in between pores, and around hard ferrite grains. Additionally, the KAM (kernel average misorientation) map of the selected area indicates accumulation of dislocation based plastic deformation of austenite in areas adjacent to hard ferrite grain (Fig. 10d). The increase in twinning intensity is followed by martensite α' nucleation and growth. The prevalence of phase transformation around the porosity, suggest that martensite formation can act as strengthening mechanism around the pores, resulting in delocalization of deformation away from those areas. The relatively harder ferrite grains appear to be stable through the entire tensile test and are mostly undeformed until failure. The KAM map indicates some strain transfer from austenite into the ferrite grains, which can be

transferred further into next austenite grain (Fig. 10d).

The uniaxial tensile test of the FFF 316L steel to failure at 77 K results in almost complete transformation of austenite grains into martensite α' (Fig. 11b and c). After the failure, only small austenite grains (around 2 μm diameter) are retained in between the martensite laths. The microstructure of martensite α' consists of heavily twinned and deformed laths resulting in relatively fine BCC grains. Grain boundaries in martensite phase mostly exhibit twin like or needle morphology, however not all of them match the $\Sigma3\,\langle111\rangle\,60^\circ$ misorientation. Most of the martensite grains also have internal structure evident in increased KAM values as well as high density of low angle grain boundaries (LAGB), indicating dislocation slip activity. Similarly to tensile test at room temperature, the ferrite grains appear relatively undeformed in comparison to prior austenite grains. However, some deformation and therefore dislocation accumulation observed in KAM map is observed (Fig. 11d). Additionally, ferrite islands in close proximity to pores, some deformation accommodation is also observed through increased KAM values and LAGB accumulation (Fig. 11c).

Microstructure observed in an area of the FFF 316L deformed sample with higher cross section area, and therefore lower imposed strain, reveals an intermediate stage of deformation induced phase transformation (Fig. 11a). Initially the austenite grains deform only through narrow deformation twins and along those twin boundaries a twinned martensite can start to appear. However mostly the deformation induced martensite appears to nucleate without austenite twin boundaries.

Depending on the initial austenite grain orientation, the martensite can appear either as narrow intersecting needles (Fig. 12a) or widening bands (Fig. 12c). In all observed cases the martensite transformation occurs with the intermediate hcp ε phase, which then transforms to twinned martensite α'. As mentioned the narrow needle-like martensite can appear without twinning in prior austenite grain, however typically the needles occur with some prior dislocation activity, which can be observed either as a faint line in band contrast (BC) or in KAM maps (Fig. 12a and b). The growing martensite needles can be interrupted by existing twin boundaries, however the strain can be transmitted through the boundary and secondary strain induced martensite needle can be formed inside the twinned area (Fig. 12a). On the other hand, the widening laths of twinned martensite impose some strain on the surrounding areas which is accommodated by dislocation glide in prior austenite (Fig. 12c and d). At this stage both martensite and austenite appears mostly deformation free in the KAM maps (Fig. 12b and d), which suggest that the dislocation structures observed after the fracture (Fig. 11d) are accumulated after the microstructure is completely transformed to martensite. Ferrite islands at this early stage of deformation does not present any deformation accommodation or dislocation activity in KAM contrast (Fig. 12b). This is due to the lack of easy slip systems in ferrite.

It is worth noting that during the uniaxial tensile test at 77 K, a Lüders-like effect (Fig. 4) is observed in conventional 316L stainless steel [53,57]. Nevertheless, despite this behaviour, the microstructure evolution of conventional 316L shows some notable similarities to that of the FFF 316L sample. Before strain localization (outside of the front) the austenite grains deform through dislocation glide and limited mechanical twinning. Similarly, to the FFF 316L martensite first appear as narrow needles or as slightly wider bands. Depending on prior austenite grain orientation, the needles appear either oriented in single direction or are intersecting each other. Martensite also nucleates at existing twin boundaries, or at areas close to grain boundary triple points, where more intensive shearing is most likely to occur (Fig. 13a). Inside of the deformation front, additional martensite needles appear, while the existing ones are widening and merging with each other (Fig. 13b). Moreover, the martensite transformation occurs with the intermediate ε

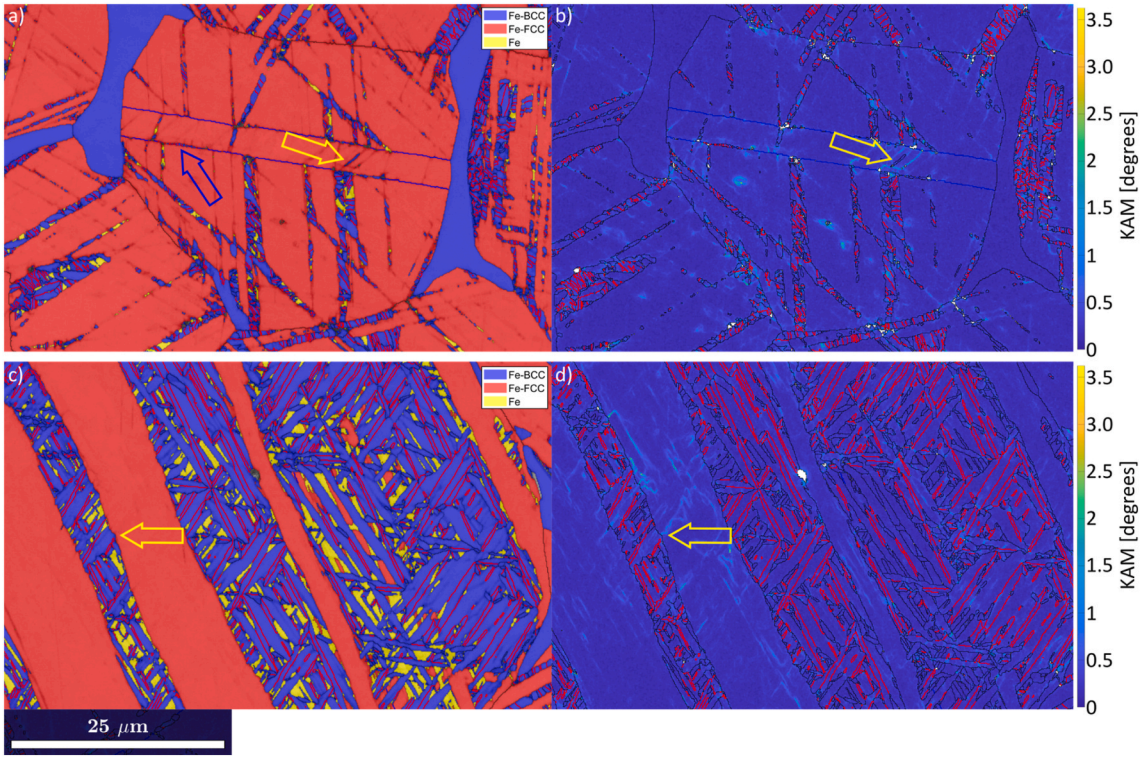

Fig. 12. Magnification of area indicated in Fig. 11 (showing initial deformation at 77 K): phase maps plus BC on the left and KAM maps on the right; blue lines indicate Σ3 boundary in austenite; red lines indicate Σ3 boundary in martensite; arrow in (a) and (b) indicate strain transfer through a twinned area as a result of growing martensite lath interaction with twin boundary and resulting martensite nucleation inside the twin region; arrows in (c) and (d) indicate strain accommodation in austenite as a result of twinning occurring in a martensite lath; blue arrow indicates formation of twinned martensite along an austenite Σ3 boundary. Please refer to full resolution image for detailed analysis. (For interpretation of the references to colour in this figure legend, the reader is referred to the Web version of this article.)

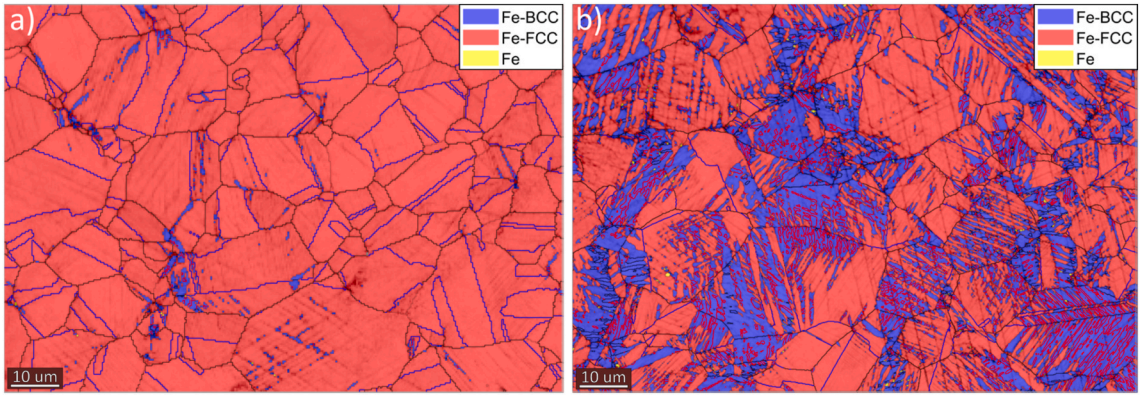

Fig. 13. Phase distribution maps of conventional 316L samples after tension at 77 K: outside of the deformation front (a) and inside of the front (b).

phase, however the retention of this phase in the microstructure is much lower in the conventional sample. In this case multiple twin boundaries in the martensite α' are also observed, however not as numerous as in the FFF 316L.

The microstructure evolution of conventional 316L and FFF 316L can be compared by relating the grain boundary (GB) densities in the austenite and martensite with relative concentrations of those two phases. The grain boundary densities have been calculated in areas of the microstructure with varying fractions of austenite and martensite (FCC and BCC phases respectively) and presented in bar plots in Figs. 14 and 15. In both cases the overall grain boundary density increases with increasing concentration of the BCC phase (increasing martensite content). In FFF 316L austenite boundaries accumulate strongly with increasing deformation and BCC phase content, the LAGB (low-angle grain boundaries) and HAGB (high-angle grain boundaries) boundary densities increase at a similar rate.

The increase in HAGB density in FFF 316L sample is related to mechanical twinning. In BCC phases grain boundary evolution occurs mostly in martensite, whereas delta ferrite grains are mostly unchanged. In austenite initial density of GB in FFF 316L is low (Figs. 14c–1 RT) due to relatively large grain size, however with deformation at RT the value increases and at fracture is higher (Figs. 14c–4 RT) than in 77 K deformed conventional 316L sample (Fig. 15c). In the BCC phase the GB evolution at RT is also observed in newly formed martensite. At 77 K after fracture the GB density in BCC is over 4 times higher in the FFF 316L sample than in conventional 316L (Figs. 14b–3 LN and Figs. 15b–9). However, in FFF 316L the twin boundaries are a much lower fraction of overall GBs compared to conventional 316L, despite previously mentioned higher density of twin boundaries in martensite forming in early stages of FFF 316L deformation. This indicates that during tensile testing at 77 K the twin boundary formation occurs relatively early in FFF 316L, and the following deformation occurs through dislocation activity, leading to accommodation of misorientations, transforming the twin boundaries into random high angle grain boundaries. This is due to the different chemical composition of austenite in the conventional 316L and FFF 316L samples, which affects the stacking fault energy (see Fig. 4).

4. Discussion

The current study aimed to compare the mechanical behaviour of FFF 316L and conventional 316L ASS under room temperature and cryogenic conditions (77 K), focusing on the role of DIMT. The results confirm the hypothesis that DIMT behaves differently in the two materials, particularly under cryogenic conditions, with implications for their respective mechanical properties and applications. At 77 K, the Lüders-like effect associated with DIMT was observed in conventional 316L, consistent with prior work [61]. However, no Lüders-like effect was detected in FFF 316L at the same temperature. This divergence can be attributed not only to the chemical composition of austenite but also to the presence of porosities in FFF 316L, which hinder the propagation of martensitic fronts throughout the specimen.

In room temperature tests, the RMS-based method [50] revealed a uniform strain distribution in conventional 316L, which correlated with the distribution of DIMT during loading-unloading cycles. For FFF 316L, martensitic nucleation was predominantly observed around pores, aligning with observations in similar materials [32]. These localized transformations suggest a strengthening mechanism unique to FFF 316L, as the porosities act as stress concentrators for martensitic formation (Fig. 10c).

It is worth pointing out that in the FFF 316L specimens, initial Fe-δ islands were observed at grain boundaries, attributed to the fabrication process. Moreover, these islands remain undeformed during tensile loading, reinforcing the classification of FFF 316L as a multiphase material. Future research should focus on understanding their impact on yield stress, total elongation, and corrosion resistance. Additionally, optimizing fabrication parameters to control ferrite content and porosity could further enhance the potential of FFF 316L for specific applications. Kurzynowski et al. [62] investigated the effects of various SLM (selective laser melting) processing parameters, including laser power and scanning strategies, on the microstructure and texture of the specimens. The microstructures of the as-built specimens were characterized by

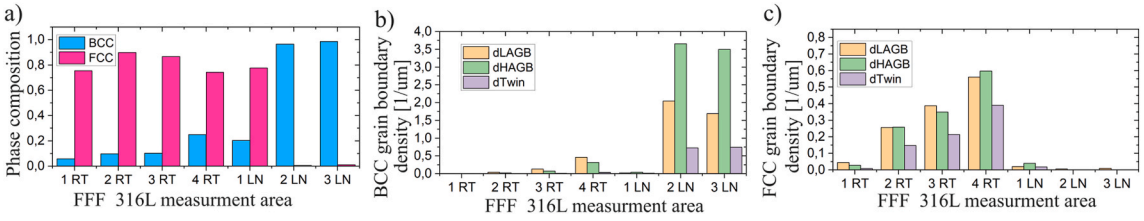

Fig. 14. Grain boundary densities in the (b) BCC and (c) FCC phases with respect to relative phase volume fraction (a) at areas of the microstructure in FFF 316L. RT – tensile tested at room temperature; LN – tensile tested at 77 K; consecutive numbers refer to EBSD maps collected in areas with different deformation, and sorted with increasing volume fraction of the BCC phase.

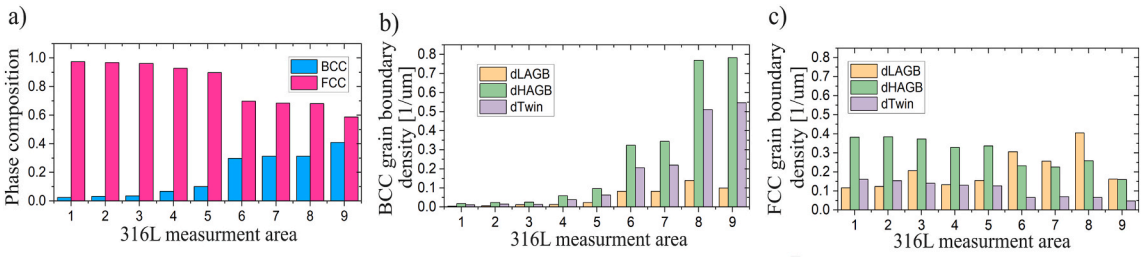

Fig. 15. Grain boundary densities in the (b) BCC and (c) FCC phases with respect to relative phase volume fraction (a) at areas of the microstructure in conventional 316L; all measurements taken after tensile testing at 77 K; consecutive numbers refer to EBSD maps collected in areas with different deformation, and sorted with increasing volume fraction of the BCC phase.

columnar austenite grains with intercellular segregation of Mo, Cr, and Si, leading to the formation of non-equilibrium peritectic ferrite. It was observed that the laser energy density and scanning strategy significantly influenced the cellular substructure of austenite, the quantity of ferrite, and the type and intensity of the texture.

The different mechanical behaviour of the FFF 316L and conventional 316L steels at 77 K seem to be affected by several microstructural factors. First, the austenite grains in FFF 316L are considerably larger than in conventional 316L and have altered chemical composition due to some of chromium and molybdenum concentrating in the ferrite islands. The grain size dependence of the mechanical stability of austenite, was studied by Ref. [63] in metastable ASS, with grain sizes ranging from 1 to 80 μm. The results revealed that mechanical stability of austenite is grain size independent, as advantageous martensite variants are preferentially selected during transformation to accommodate tensile strain. Therefore, while grain size does not influence the DIMT, differences in chemical composition have the effect of higher propensity of FFF 316L austenite to transform to martensite, resulting in relatively early phase transformation, and overall larger fraction of martensite at the end of tensile test compared to conventional 316L. This in turn can affect the Lüders effect and the so called 'front propagation', which as shown by Nalepka et al. [53], is related to coordinated martensite formation in austenite grains with Cu and Goss-Brass orientations evolved in prior dislocation based deformation stages. As the martensite in FFF 316L can evolve relatively easily and early, the Cu and Goss-Brass oriented grains does not have the opportunity to develop, and thus cannot contribute to coordinated martensite formation in Lüders like behaviour or 'front propagation'. Moreover the FFF 316L steel contains both porosities and ferrite islands, which as shown here affect the mechanical response of neighbouring austenite grains by locally inducing martensite transformation and creating areas of strain concentration respectively. By locally inducing the DIMT relatively early in the deformation process, the pores decrease the ability of material to transform in a coordinated manner and prevents the occurrence of deformation instability or Lüders like behaviour later in the tensile test (see Fig. 16).

Conventional 316L consistently demonstrated superior mechanical properties, including higher yield stress and greater total elongation, across both room temperature and cryogenic conditions. Despite this, the strength of FFF 316L is satisfactory for applications involving fewer demanding loads, particularly for cryogenic environments. Additionally, the absence of the Lüders-like effect in FFF 316L could be advantageous in applications requiring stable hardening, where unpredictable strain-induced transformations are undesirable. The specimen printed in a 0°/90° orientation exhibits slightly higher ductility compared to the 45°/45° orientation during strain rate-controlled uniaxial tensile tests at both room and cryogenic temperatures. Thus, FFF 316L parts have the potential to serve as viable alternatives to their conventional counterparts. This is particularly true for secondary applications, such as non-structurally critical components or parts [39,40,43]. In the case of wet

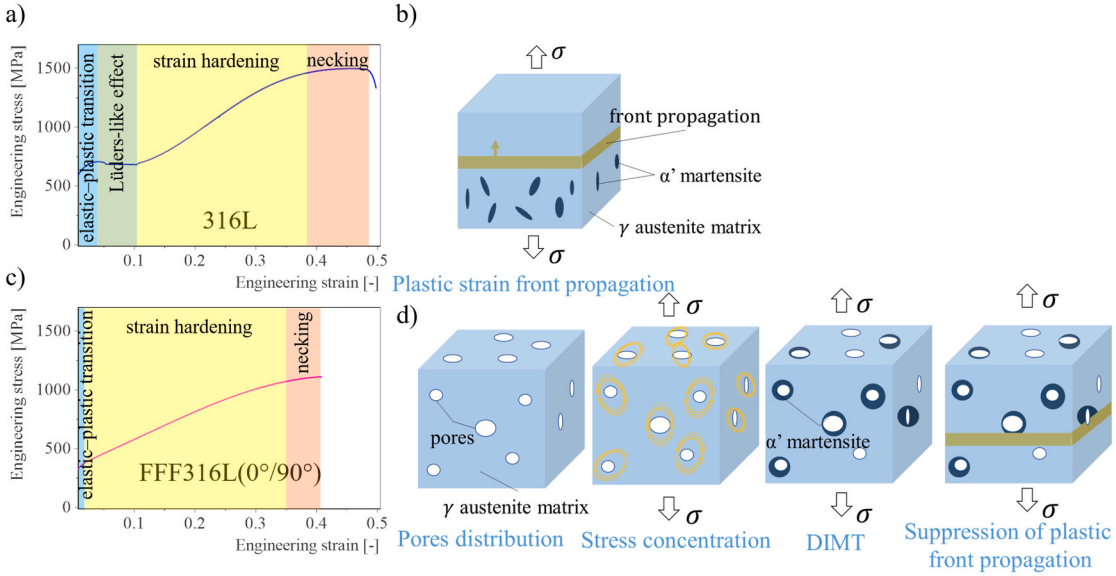

Fig. 16. Schematic illustration of the mechanism suppressing plastic strain-front propagation in FFF 316L stainless steel. (a) Stress–strain curve of conventionally processed 316L at 77 K showing a Lüders-like yield plateau; (b) schematic representation of Lüders-band propagation during plastic deformation; (c) stress–strain curve of FFF 316L at 77 K exhibiting a continuous, smooth transition without a distinct yield plateau; (d) schematic visualization of how pores and interlayer interfaces locally arrest strain localization, suppressing the formation and propagation of a Lüders-like deformation band.

corrosion operating conditions, further research is needed on the volume fraction, size, and morphology of delta ferrite precipitates and the corrosion resistance of additively produced 316L steel.

5. Conclusions

The aim of this study is to gain a comprehensive understanding of the mechanical properties of FFF 316L stainless steel across a wide temperature range (77 K and room temperature), with a particular focus on DIMT. Based on the findings, the following conclusions were drawn:

- The EBSD analysis confirmed the absence of preferential grain orientation in the microstructure of FFF 316L, indicating that the printing technology does not influence the resulting grain direction.
- Based on the procedure recommended by company for printing in FFF technology, Fe-δ forms at the grain boundaries after final samples. The ferrite content in the specimens after sintering is about 6–7 %. It is assumed that ferrite forms from the liquid phase during the high-temperature sintering step in the manufacturing process of FFF 316L. As a result, the austenite grains have relatively lower amounts of chromium and molybdenum compared to conventional 316L steel.
- During uniaxial tension tests at 77 K, martensite evolution is similar in both conventional 316L and FFF 316L specimens. However, at room temperature the behaviour diverges significantly. After the first loading–unloading cycle, the martensite volume fraction in the AM specimen increases to 2.5 % and 3.1 %, while it remains close to 0 % in the conventional specimen.
- An RMS-based strain parameter was introduced to quantify the uniformity of strain distribution during tensile loading. It was found that, under room temperature conditions, the strain distribution in conventional 316L stainless steel is more uniform than in FFF 316L. This difference is attributed to the strain concentration around pours in the FFF specimens.
- Conventional 316L exhibits plastic flow instability at 77 K, manifested by propagation of the plastic front combined with martensite evolution (Lüders-like effect). The different chemical composition of austenite grains in FFF 316L is affecting the stacking fault energy and enhancing the DIMT, while the presence of porosity and δ-ferrite precipitates are most likely responsible for the lack of plastic front propagation in the FFF printed sample.
- DIMT in FFF 316L is localized around the pores, increasing the strength of the specimen with porosity.
- At 77 K the microstructure evolution of FFF 316L sample occurs through development of twinned martensite laths, followed by dislocation glide until fracture.

CRediT authorship contribution statement

J. Tabin: Writing – original draft, Visualization, Validation, Software, Methodology, Investigation, Funding acquisition, Conceptualization. **J. Kawałko:** Writing – original draft, Visualization, Validation, Methodology, Investigation, Conceptualization. **D. Schob:** Writing – original draft, Visualization, Resources, Funding acquisition, Conceptualization. **R. Roszak:** Writing – original draft, Visualization, Resources, Conceptualization. **A. Brodecki:** Validation, Software, Investigation, Data curation. **P. Bała:** Writing – review & editing, Supervision. **Ph Maasch:** Writing – review & editing, Software. **Z. Kowalewski:** Writing – review & editing, Supervision. **M. Ziegenhorn:** Writing – review & editing, Supervision.

Declaration of competing interest

The authors declare the following financial interests/personal relationships which may be considered as potential competing interests: Jakub Tabin reports financial support and equipment, drugs, or supplies were provided by National Science Centre Poland. Jakub Tabin reports financial support and travel were provided by Polish National Agency for Academic Exchange. Daniela Schob reports financial support and travel were provided by German Academic Exchange Service. Jakub Kawalko reports financial support and equipment, drugs, or supplies were provided by Excellence Initiative - Research University. If there are other authors, they declare that they have no known competing financial interests or personal relationships that could have appeared to influence the work reported in this paper.

Acknowledgements

This work has been supported by the National Science Centre through Grant No UMO-2023/51/D/ST8/02370 and Polish National Agency for Academic Exchange through Grant No BPN/BDE/2023/1/00022/U/00001/ZU/00001. The research results presented in this paper have been developed using equipment financed from the funds of the “Excellence Initiative - Research University” program at AGH University of Krakow. This work has been supported by the DAAD - Deutscher Akademischer Austauschdienst for the project: “Experimental investigation and thermomechanical modelling of the material and damage behaviour for additive manufactured austenitic stainless steels under cryogenic conditions” - project number: 57703224.

Data availability

Data will be made available on request.

References

[1] H. Fujita, T. Katayama, In-situ observation of strain-induced gamma-epsilon-alpha prime and gamma-alpha prime martensitic transformation in Fe-Cr-Ni alloys, Mater. Trans. JIM (33) (1992) 243–252.
[2] K. Nalepka, B. Skoczeń, R. Schmidt, W. Zwolińska-Faryj, E. Schmidt, R. Chulist, Physical mechanism of the intermittent plastic flow at extremely low temperatures, Int. J. Plast. 177 (2024) 103994.
[3] Y.-K. Kim, S.-W. Kim, K.R. Lim, Y.-S. Na, Enhancing strength-ductility synergy in 316L stainless steel through pre-straining at 4.2K, Mater. Sci. Eng., A 906 (2024) 146709.
[4] S. Wu, J. Xin, W. Xie, H. Zhang, C. Huang, W. Wang, Z. Zhou, Y. Zhou, L. Li, Mechanical properties and microstructure evolution of cryogenic pre-strained 316LN stainless steel, Cryogenics 121 (2022) 103388.
[5] B. Skoczeń, J. Bielski, J. Tabin, Multiaxial constitutive model of discontinuous plastic flow at cryogenic temperatures, Int. J. Plast. 55 (2014) 198–218.
[6] P. Czarkowski, A.T. Krawczynska, R. Slesinski, T. Brynk, J. Budniak, M. Lewandowska, K.J. Kurzydlowski, Low temperature mechanical properties of 316L type stainless steel after hydrostatic extrusion, Fusion Eng. Des. 86 (9) (2011) 2517–2521.
[7] D. Harshini, A.u. Haq, T. Buddi, K. Ajay Kumar, A. Anitha Lakshmi, Comparative study on mechanical behavior of ASS 316L for low and high temperature applications, Mater. Today Proc. 19 (2019) 767–771.
[8] M. Kothari, S. Niu, V. Srivastava, A thermo-mechanically coupled finite strain model for phase-transitioning austenitic steels in ambient to cryogenic temperature range, J. Mech. Phys. Solid. 133 (2019) 103729.
[9] M.R. Crivoi, J.J. Hoyos, M.T. Izumi, D.J.M. de Aguiar, R.S. Namur, A.L. Terasawa, O.M. Cintho, In situ analysis of cryogenic strain of AISI 316L stainless steel using synchrotron radiation, Cryogenics 105 (2020) 103020.
[10] J. Tabin, Strain measurement by means of clip-on extensometers during discontinuous plastic flow at 4 K, Cryogenics 123 (2022) 103451.
[11] J. Tabin, B. Skoczeń, J. Bielski, Discontinuous plastic flow in stainless steels subjected to combined loads at extremely low temperatures, Int. J. Mech. Sci. 200 (2021) 106448.
[12] G.B. Olson, M. Cohen, A mechanism for the strain-induced nucleation of martensitic transformations, J. Less Common Metals 28 (1) (1972) 107–118.
[13] J. Tabin, B. Skoczen, J. Bielski, Discontinuous plastic flow coupled with strain induced fcc–bcc phase transformation at extremely low temperatures, Mech. Mater. 129 (2019) 23–40.
[14] J. Talonen, Effect of strain-induced α’-martensite Transformation on Mechanical Properties of Metastable Austenitic Stainless Steels, 2007, p. 127. Phd Thesis.
[15] W.S. Park, M.S. Chun, M.S. Han, M.H. Kim, J.M. Lee, Comparative study on mechanical behavior of low temperature application materials for ships and offshore structures: part I—experimental investigations, Mater. Sci. Eng., A 528 (18) (2011) 5790–5803.
[16] W.S. Park, S.W. Yoo, M.H. Kim, J.M. Lee, Strain-rate effects on the mechanical behavior of the AISI 300 series of austenitic stainless steel under cryogenic environments, Mater. Des. 31 (8) (2010) 3630–3640.
[17] P.L. Mangonon, G. Thomas, The martensite phases in 304 stainless steel, Metall. Trans. A 1 (6) (1970) 1577–1586.

[18] V. Mertinger, E. Nagy, F. Tranta, J. Sólyom, Strain-induced martensitic transformation in textured austenitic stainless steels, Mater. Sci. Eng., A 481–482 (2008) 718–722.
[19] T. Suzuki, H. Kojima, K. Suzuki, T. Hashimoto, M. Ichihara, An experimental study of the martensite nucleation and growth in 18/8 stainless steel, Acta Metall. 25 (10) (1977) 1151–1162.
[20] A.A. Lebedev, V.V. Kosarchuk, Influence of phase transformations on the mechanical properties of austenitic stainless steels, Int. J. Plast. 16 (7) (2000) 749–767.
[21] K. Sato, M. Ichinose, Y. Hirotsu, Y. Inoue, Effects of deformation induced phase transformation and twinning on the mechanical properties of austenitic fe–mn–al alloys, ISIJ Int. 29 (10) (1989) 868–877.
[22] B. Sun, Y. Pan, J. Yang, J. Guo, B. Zhao, X. Liu, Z. Liu, X. Li, Microstructure evolution and SSCC behavior of strain-strengthened 304 SS pre-strained at room temperature and cryogenic temperature, Corros. Sci. 210 (2023) 110855.
[23] L. Chang, M.G. Burke, K. Mukahiwa, J. Duff, Y. Wang, F. Scenini, The effect of martensite on stress corrosion crack initiation of austenitic stainless steels in high-temperature hydrogenated water, Corros. Sci. 189 (2021) 109600.
[24] M.J. Gomes da Silva, H.A.P. Fragoso, R.C.A.G. Barrio, J.L. Cardoso, Stress corrosion of an austenitic stainless steel expansion joint, a case study, Eng. Fail. Anal. 97 (2019) 300–310.
[25] I. Janeiro, O. Hubert, J.-H. Schmitt, In-situ strain induced martensitic transformation measurement and consequences for the modeling of medium Mn stainless steels mechanical behavior, Int. J. Plast. 154 (2022) 103248.
[26] B. Cao, T. Iwamoto, P.P. Bhattacharjee, An experimental study on strain-induced martensitic transformation behavior in SUS304 austenitic stainless steel during higher strain rate deformation by continuous evaluation of relative magnetic permeability, Mater. Sci. Eng., A 774 (2020) 138927.
[27] W. Stautner, S. Vanapalli, K.P. Weiss, R. Chen, K. Amm, E. Budesheim, J. Ricci, The scope of additive manufacturing in cryogenics, component design, and applications, IOP Conf. Ser. Mater. Sci. Eng. 278 (1) (2017) 012134.
[28] T. DebRoy, H.L. Wei, J.S. Zuback, T. Mukherjee, J.W. Elmer, J.O. Milewski, A. M. Beese, A. Wilson-Heid, A. De, W. Zhang, Additive manufacturing of metallic components – process, structure and properties, Prog. Mater. Sci. 92 (2018) 112–224.
[29] J. Jansa, A. Volodarskaja, J. Hlinka, L. Zárybnická, S. Polzer, M. Kraus, J. Hajnyš, D. Schwarz, M. Pagáč, Corrosion and material properties of 316L stainless steel produced by material extrusion technology, J. Manuf. Process. 88 (2023) 232–245.
[30] N. Iqbal, E. Jimenez-Melero, U. Ankalkhope, J. Lawrence, Microstructure and mechanical properties of 316L stainless steel fabricated using selective laser melting, MRS Adv. 4 (44) (2019) 2431–2439.
[31] C. Wang, X. Lin, L. Wang, S. Zhang, W. Huang, Cryogenic mechanical properties of 316L stainless steel fabricated by selective laser melting, Mater. Sci. Eng., A 815 (2021) 141317.
[32] S.G. Jeong, E.S. Kim, H. Kwon, S.Y. Ahn, J. Choe, G.M. Karthik, Y.-U. Heo, H. S. Kim, Tailoring deformation-induced martensitic transformation through cellular engineering in laser powder bed fusion processed 316L stainless steel, Mater. Sci. Eng., A 898 (2024) 146383.
[33] Y. Hong, C. Zhou, S. Wagner, S. Schlabach, A. Pundt, L. Zhang, J. Zheng, Strain-induced twins and martensite: effects on hydrogen embrittlement of selective laser melted (SLM) 316 L stainless steel, Corros. Sci. 208 (2022) 110669.
[34] G. Wu, N.A. Langrana, R. Sadanji, S. Danforth, Solid freeform fabrication of metal components using fused deposition of metals, Mater. Des. 23 (1) (2002) 97–105.
[35] M.K. Agarwala, R.v. Weeren, A. Bandyopadhyay, A. Safari, S.C. Danforth, W. R. Priedeman, Filament feed materials for fused deposition processing of ceramics and metals. 1996 International Solid Freeform Fabrication Symposium, 1996.
[36] J. Gonzalez-Gutierrez, S. Cano, S. Schuschnigg, C. Kukla, J. Sapkota, C. Holzer, Additive manufacturing of metallic and ceramic components by the material extrusion of highly-filled polymers: a review and future perspectives, Materials 11 (5) (2018) 840.
[37] M. Bragaglia, M. Mariani, C. Sergi, F. Sarasini, J. Tirillò, F. Nanni, Polylactic acid as biobased binder for the production of 3D printing filaments for Ti6Al4V alloy manufacturing via bound metal deposition, J. Mater. Res. Technol. 27 (2023) 168–181.
[38] S. Spiller, S. Olsøybakk Kolstad, N. Razavi, Fatigue behavior of 316L stainless steel fabricated via material extrusion additive manufacturing, Eng. Fract. Mech. 291 (2023) 109544.
[39] M.Á. Caminero, A. Romero, J.M. Chacón, P.J. Núñez, E. García-Plaza, G. P. Rodríguez, Additive manufacturing of 316L stainless-steel structures using fused filament fabrication technology: mechanical and geometric properties, Rapid Prototyp. J. 27 (3) (2021) 583–591.
[40] H. Gong, D. Snelling, K. Kardel, A. Carrano, Comparison of stainless steel 316L parts made by FDM- and SLM-based additive manufacturing processes, JOM 71 (3) (2019) 880–885.
[41] F. Wang, S. You, D. Jiang, X. Yuan, R. Fu, F. Ning, Microstructure evolution, phase formation, corrosion, and mechanical properties of stainless steel fabricated by extrusion-based sintering-assisted additive manufacturing, Addit. Manuf. 75 (2023) 103746.
[42] J. Damon, S. Dietrich, S. Gorantla, U. Popp, B. Okolo, V. Schulze, Process porosity and mechanical performance of fused filament fabricated 316L stainless steel, Rapid Prototyp. J. 25 (7) (2019) 1319–1327.
[43] S.O. Obadimu, A. Kasha, K.I. Kourousis, Tensile performance and plastic anisotropy of material extrusion steel 316L: influence of primary manufacturing parameters, Addit. Manuf. 60 (2022) 103297.
[44] Y. Thompson, J. Gonzalez-Gutierrez, C. Kukla, P. Felfer, Fused filament fabrication, debinding and sintering as a low cost additive manufacturing method of 316L stainless steel, Addit. Manuf. 30 (2019) 100861.
[45] J.L. Betts, B.J. Sampson, K. Lindsey, F.M. Brinkley, M.W. Priddy, Reduction of process induced porosity for ultrafuse 316L through parameter optimization of creality ender 3 V2 and makerbot method X, Crystals 14 (3) (2024) 285.
[46] S.H. Ahn, M. Montero, D. Odell, S. Roundy, P.K. Wright, Anisotropic material properties of fused deposition modeling ABS, Rapid Prototyp. J. 8 (4) (2002) 248–257.
[47] G. Gao, F. Xu, J. Xu, G. Tang, Z. Liu, A survey of the influence of process parameters on mechanical properties of fused deposition modeling parts, Micromachines 13 (4) (2022) 553.
[48] J. Talonen, P. Aspegren, H. Hänninen, Comparison of different methods for measuring strain induced α-martensite content in austenitic steels, Mater. Sci. Technol. 20 (12) (2004) 1506–1512.
[49] F. Bachmann, R. Hielscher, H. Schaeben, Texture analysis with MTEX – free and open source software toolbox, Solid State Phenom. 160 (2010) 63–68.
[50] J. Tabin, A. Brodecki, Parametrisation of uniform deformation in ductile metals using digital image correlation technology. Experimental Techniques, 2024.
[51] J. Tabin, Kinematic and thermal characteristic of discontinuous plastic flow in metastable austenitic stainless steels, Mech. Mater. 163 (2021) 104090.
[52] J. Tabin, M. Prącik, Methods for identifying dynamic parameters of clip-on extensometer–specimen structure in tensile tests, Measurement 63 (2015) 176–186.
[53] K. Nalepka, J. Tabin, J. Kawałko, A. Brodecki, P. Bała, Z. Kowalewski, Plastic flow instability in austenitic stainless steels at room temperature: macroscopic tests and microstructural analysis, Int. J. Plast. (2024) 104159.
[54] S. Kedziora, T. Decker, E. Museyibov, J. Morbach, S. Hohmann, A. Huwer, M. Wahl, Strength properties of 316L and 17-4 PH stainless steel produced with additive manufacturing, Materials (Basel, Switzerland) (2022) 6278.
[55] K. Nalepka, B. Skoczeń, M. Ciepielowska, R. Schmidt, J. Tabin, E. Schmidt, W. Zwolińska-Faryj, R. Chulist, Phase transformation in 316L austenitic steel induced by fracture at cryogenic temperatures: experiment and modelling, Materials 14 (1) (2021) 127.
[56] J.L. Wang, M.H. Huang, X.H. Xi, C.C. Wang, W. Xu, Characteristics of nucleation and transformation sequence in deformation-induced martensitic transformation, Mater. Char. 163 (2020) 110234.
[57] S. Gao, Y. Bai, R. Zheng, Y. Tian, W. Mao, A. Shibata, N. Tsuji, Mechanism of huge Lüders-type deformation in ultrafine grained austenitic stainless steel, Scr. Mater. 159 (2019) 28–32.
[58] R. Santamaria, M. Salasi, S. Bakhtiari, G. Leadbeater, M. Iannuzzi, M.Z. Quadir, Microstructure and mechanical behaviour of 316L stainless steel produced using sinter-based extrusion additive manufacturing, J. Mater. Sci. 57 (21) (2022) 9646–9662.
[59] A. Yadollahi, N. Shamsaei, S.M. Thompson, D.W. Seely, Effects of process time interval and heat treatment on the mechanical and microstructural properties of direct laser deposited 316L stainless steel, Mater. Sci. Eng., A 644 (2015) 171–183.
[60] D.G. Brandon, The structure of high-angle grain boundaries, Acta Metall. 14 (11) (1966) 1479–1484.
[61] J. Tabin, K. Nalepka, J. Kawałko, A. Brodecki, P. Bała, Z. Kowalewski, Plastic flow instability in 304 austenitic stainless steels at room temperature, Metall. Mater. Trans. 54 (12) (2023) 4606–4611.
[62] T. Kurzynowski, K. Gruber, W. Stopyra, B. Kuźnicka, E. Chlebus, Correlation between process parameters, microstructure and properties of 316 L stainless steel processed by selective laser melting, Mater. Sci. Eng., A 718 (2018) 64–73.
[63] Y. Matsuoka, T. Iwasaki, N. Nakada, T. Tsuchiyama, S. Takaki, Effect of grain size on thermal and mechanical stability of austenite in metastable austenitic stainless steel, ISIJ Int. 53 (7) (2013) 1224–1230.